Available online at www.sciencedirect.com
ScienceDirect
Trans. Nonferrous Met. Soc. China 33(2023) 1398−1410
Transactions of Nonferrous Metals Society of China
www.tnmsc.cn

Corrosion behavior of as-cast AZ91 magnesium alloy with VN particle additions in NaCl solution

Wei QIU[1,2], Ya-wen LI[1,2], Gang HUANG[1,2], Jian CHEN[1,2], Yan-jie REN[1,2], Wei-ying HUANG[1,2], Wei CHEN[1,2], Tang-qing WU[3], Mao-hai YAO[4], Ai-hu XIONG[4]

1. School of Energy and Power Engineering, Changsha University of Science & Technology, Changsha 410114, China;
2. Key Laboratory of Energy Efficiency and Clean Utilization, the Education Department of Hunan Province, Changsha University of Science & Technology, Changsha 410114, China;
3. School of Materials Science and Engineering, Xiangtan University, Xiangtan 411105, China;
4. Institute of Rare Earth Light Alloys, Hunan Rare Earth Metal Material Research Institute, Changsha 410126, China

Received 26 December 2021; accepted 31 May 2022

Abstract: The microstructures and corrosion behavior of the as-cast AZ91−xVN (x=0, 0.25, 0.5 and 1 in wt.%) alloys were investigated using optical microscopy (OM), X-ray diffraction (XRD), scanning electron microscopy (SEM) and electrochemical measurements. The results showed that VN can significantly refine and modify the microstructures of AZ91−xVN alloys. The corrosion resistance of the AZ91 alloy was first improved and then deteriorated with the addition of VN particles. The superior corrosion resistance of the as-cast AZ91−0.25VN alloy with the lowest corrosion rate (P_W=(1.47±0.06) mm/a) was attributed to the additional grain boundaries. With the further increase of VN content, the amount of the lamellar β-$Mg_{17}Al_{12}$ precipitation phase increased, and thus the galvanic corrosion between β phase and the α-Mg matrix was promoted, resulting in the deteriorated corrosion resistance of the alloys.
Key words: AZ91−xVN alloys; microstructure; grain refinement; corrosion resistance

1 Introduction

High energy efficiency and low emission materials are always desirable, especially under the current challenge of worldwide energy crisis and environmental pollution. Therefore, there is considerable interest in the design and development of lightweight and energy efficient materials [1]. Among them, magnesium (Mg) and its alloys, with low density (1.74 g/cm^3), high specific strength, high specific stiffness, and good electrical and thermal conductivity are ideal materials in the field of automotive, aerospace, and consumer electronics (3C) products. However, the poor corrosion resistance of the alloy still limits the large-scale industrial production of Mg-based products [2,3].

Due to the active nature and high negative potential, Mg and its alloys are susceptible to galvanic corrosion, and moreover, the porous oxide film on their surface cannot prevent the base metal from further corrosion failure [4]. There are several techniques which can improve the corrosion resistance of Mg alloys, such as surface coating techniques [5,6], alloying [7], hot deformation [8] and microstructural control [9]. Among these techniques, grain size control is one of the most feasible methods to achieve the improvement of corrosion behavior of Mg alloys [10−15]. However, the effect of grain size on the corrosion resistance of Mg alloys is not well understood. Some researchers believed that grain boundaries

Corresponding author: Yan-jie REN, Tel: +86-13657310308, E-mail: yjren@csust.edu.cn;
Tang-qing WU, Tel: +86-13875256157, E-mail: tqwu10s@alum.imr.ac.cn
DOI: 10.1016/S1003-6326(23)66191-6

were crystallographic defects, which were normally preferentially eroded, and thus grain refinement actually accelerated the corrosion rate [10,11]. In contrast, ABDEL-GAWAD and SHOEIB [12] demonstrated the negative correlation between corrosion resistance and grain size in Ca and Zn modified Mg alloys, which meant that small grain size allowed enhanced corrosion resistance. ZHANG et al [13] pointed out that the corrosion resistance of pure Mg can be significantly improved via the grain size refinement. CUBIDES et al [14] found that the corrosion performance of AZ91 alloy was improved after ECAP treatment, which was attributed to the grain refinement and the uniformly distributed β-$Mg_{17}Al_{12}$ along the grain boundaries. BUZOLIN et al [15] added CaO and RE to AZ91 alloy, which significantly refined the grain size and improved the corrosion resistance of the alloy, respectively.

Besides, as the low-cost and efficient grain refiners, nitrides have been widely applied to the microstructure control of metals by many researchers throughout the world. BACH et al [16] found that the decrease in grain size of Al-based alloy was attributed to addition of AlN. LAZAROVA et al [17] verified that the addition of 0.1 wt.% TiCN particles can significantly refine the grain size of P265GH cast steel. Recently, nitrides have been widely studied to be potential heterogeneous nucleation agents for Mg and its alloys. FU et al [18] added 0.5 wt.% AlN to AZ31 Mg alloy, and the grain size of the alloy was distinctly reduced. YANG et al [19] in situ fabricated AlN/AZ91 composites by the bubbling nitrogen method, and found that the grain size was significantly refined by the addition of AlN. ZHAO et al [20] reported that the AlN phase can act as heterogeneous nucleation sites for small-sized α-Mg grains. Similar phenomena in our previous work were also observed in the AZ31 Mg alloy with the addition of VN particles [21]. In molten metal, VN spontaneously reacted with Al to in situ generate the AlN phase, and the generated AlN and the unreacted VN particles served as the nucleation for α-Mg, thus refining the grain size. Therefore, VN might be a promising candidate for grain refinement of Mg alloy.

This work was initiated to understand the effects of the addition of VN particles on the microstructure and corrosion performance of AZ91 alloys. Then, the corrosion performance of AZ91−xVN alloys was evaluated by immersion tests, polarization curves, and electrochemical impedance spectroscopy (EIS). Meanwhile, the effects of different microstructures on the corrosion behaviors of AZ91 alloys were systematically illustrated.

2 Experimental

2.1 Materials preparation

Mg (99.9%), Al (99.9%), Zn (99.9%), Mg−10%Mn master alloys and VN particles with a diameter of 1 μm were together used to prepare the experimental materials using an electromagnetic induction furnace. The melts were protected in a CO_2 + SF_6 atmosphere, manually stirred at 750 °C for 15 min and held for 10 min, and then poured into a preheated graphite mold to obtain d85 mm × 180 mm as-cast AZ91−xVN (x=0, 0.25, 0.5 and 1 in wt.%) alloys. Center sections of ingots were taken and cut into cubic specimens of 10 mm × 10 mm × 10 mm, and some of the specimens were subjected to solid solution treatment at 420 °C for 5 h.

2.2 Microstructure characterization

The sample surfaces were ground with 400#–2000# grit SiC papers, and subsequently polished with 0.3 μm alumina slurry. Then, the as-cast alloys were etched using an etchant (1 g oxalic acid + 19 mL distilled water), and the solution-treated alloys were etched with acetic picral (2.1 g picric acid + 5 mL acetic acid + 5 mL distilled water + 35 mL alcohol). The microstructure of the alloys was observed by optical microscopy (OM, Zeiss 200 MAT) and scanning electron microscopy (SEM, FEI Quanta 250) equipped with energy dispersive spectroscopy (EDS). The phase composition was analyzed by X-ray diffraction (XRD, D8 Advance) with a scanning angle from 5° to 90° and a scanning rate of 5 (°)/min.

2.3 Corrosion immersion test

As-cast samples were encapsulated in epoxy resin and their work surfaces with an area of 1 cm × 1 cm were ground to 2000# grit using SiC papers. Then, the samples were immersed in a 3.5 wt.% NaCl solution for 24 h at room

temperature and the hydrogen gas generated during the immersion experiment was collected using the combination of an inverted funnel and a burette. At the end of the experiment, the corroded surfaces were investigated with SEM. After that, the samples were ultrasonically cleaned using 200 g/L Cr_2O_3 + 10 g/L $AgNO_3$ and anhydrous ethanol to remove corrosion products, and the mass loss of the samples was recorded using an electronic precision balance [22]. The average corrosion rate, P_W (mm/a), was transformed by the following equation [23]:

$$P_W=3.65\Delta m/\rho \quad (1)$$

where Δm is the metal mass loss rate (mg/(cm^2·d)), and ρ is the density of the sample, which is 1.74 g/cm^3.

The hydrogen evolution rate, V_H (mL/(cm^2·d)), was converted into the corresponding corrosion rate P_H (mm/a), using the following equation [24]:

$$P_H=2.279V_H \quad (2)$$

2.4 Electrochemical measurement

Electrochemical characterization was carried out in an electrochemical workstation (Zahner Zennium 40125) with a classical three-electrode system. The samples with an exposed area of 1 cm^2 were used as the working electrode, a saturated calomel electrode was used as the reference electrode, and a Pt sheet was used as the counter electrode.

The polarization tests were measured in a range from −500 to 500 mV (vs OCP) at a scan rate of 1 mV/s after the open circuit potential (OCP) was stabilized at room temperature in a 3.5 wt.% NaCl solution. The Tafel extrapolation method was used to determine the polarization curve parameters, where the corrosion current density (J_{corr}) was positively correlated with the corrosion rate (P_i, mm/a) by the following equation [25]:

$$P_i=22.85J_{corr} \quad (3)$$

EIS experiments were performed in the frequency range from 100 kHz to 10 mHz with an amplitude signal of 10 mV at an OCP. The experimental data were fitted and analyzed by using Zview software. Each electrochemical test was repeated at least three times to ensure the reproducibility of the results.

3 Results and discussion

3.1 Microstructure

Figure 1 shows the optical micrographs of the as-cast and solution-treated AZ91−xVN (x=0, 0.25, 0.5 and 1, wt.%) alloys. From Figs. 1(a−d), a large number of β-$Mg_{17}Al_{12}$ phases are distributed in the as-cast alloys with a continuous or intermittent net structure, which makes it impossible to clearly visualize grain boundaries and calculate their grain sizes. The average grain size of the AZ91 alloy is (166.95±4.37) μm, while it decreases to (54.52±2.06) μm for the AZ91−0.25VN alloy. What's more, with the further increase of VN content, the grain sizes of the AZ91−0.5VN and AZ91−1VN alloys increase to (139.25±3.75) μm and (143.84 ±3.28) μm, respectively.

Figure 2 presents the XRD patterns of the as-cast AZ91−xVN alloys. Obviously, α-Mg (PDF#89-4894) and β-$Mg_{17}Al_{12}$ (PDF#01-1128) phases exist in the AZ91 alloy, and the addition of VN results in the appearance of AlN (PDF#46-1200) phase, which is determined in previous studies [21]. In molten metal, the VN particles could react with Al to form AlN phase and V monomer. But the V element is easy to solubilize in the Mg matrix, thus no significant peak of V-containing phase is identified in the XRD pattern.

To further investigate the composition and distribution of secondary phases in the alloys, the microstructures of as-cast AZ91 alloys with different contents of VN particles and the corresponding EDS results are shown in Fig. 3. The eutectic β phase, the Al−Mn phase and the lamellar β phase are respectively confirmed at Points A, B and C, and the black particles (Points D and E) with an approximately 1:1 Al/N molar ratio are identified as AlN phase, which is consistent with XRD result. Therefore, the AZ91−xVN alloys consist of α-Mg phase, randomly distributed bulk Al−Mn phase, two kinds of morphologies of β-$Mg_{17}Al_{12}$ phases (eutectic and lamellar β phase) and a small amount of AlN phase. Most of the eutectic β phases are surrounded by lamellar β phases. Given that the eutectic is metastable in Mg−Al alloys, the supersaturated eutectic α-Mg decomposes into lamellar β phase by discontinuous precipitation at a sufficiently low cooling rate of casting [26,27].

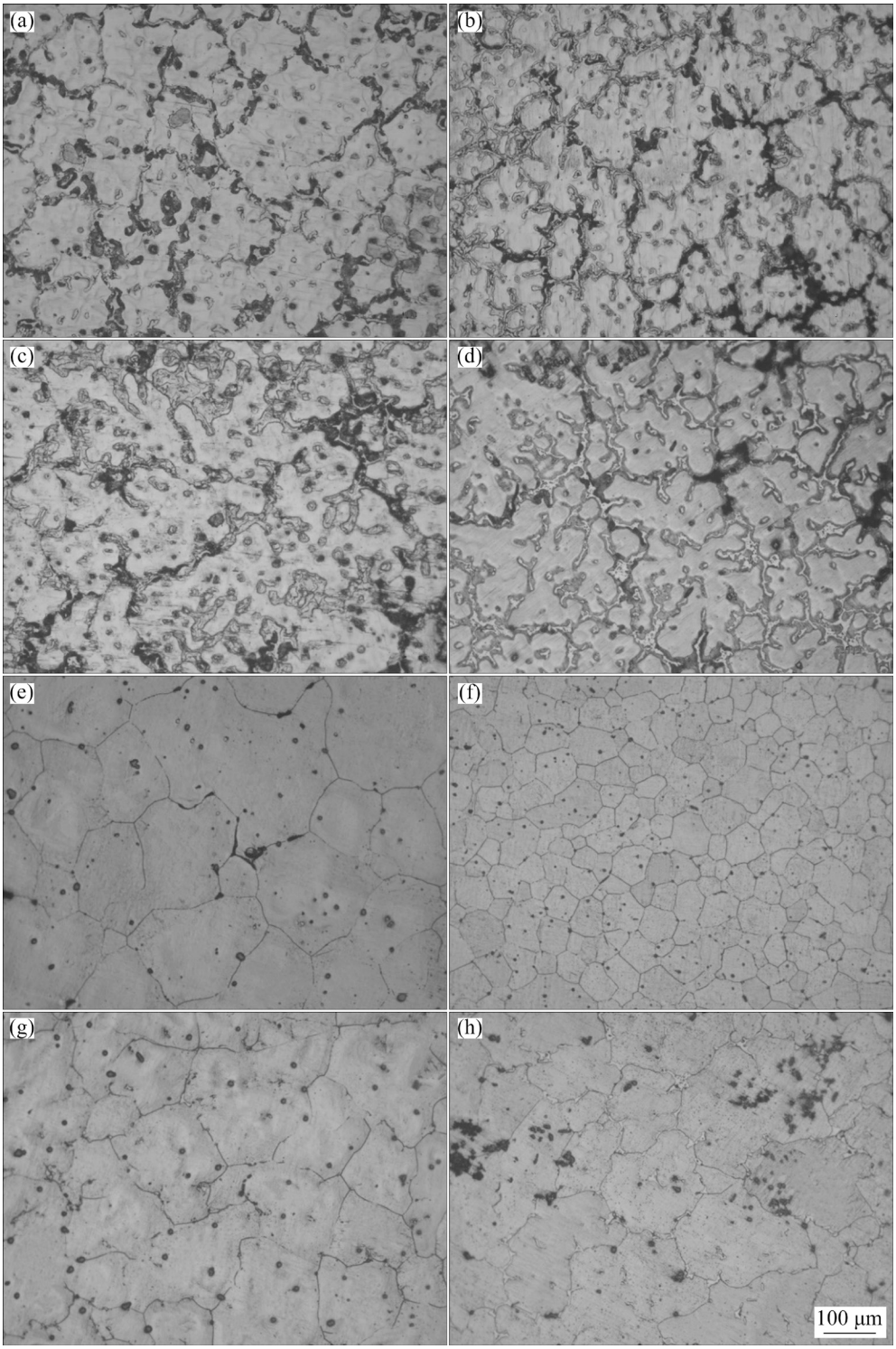

Fig. 1 Optical micrographs of AZ91−*x*VN alloys: (a−d) As-cast, *x*=0, 0.25, 0.5 and 1, respectively; (e−h) Solution-treated, *x*=0, 0.25, 0.5 and 1, respectively

Al−Mn intermetallic particles are frequently found in Mg−Al alloys due to the addition of Mn, which reduces the detrimental effect of Fe impurities on the corrosion resistance of the alloys [28]. Besides, the grain size of the AZ91−0.25VN alloy is significantly smaller than that of the unmodified AZ91 alloy, which is in keep with the OM results. The eutectic and lamellar β phases increase with the addition of 0.5% and 1% VN, and meanwhile, the AlN phase increases slightly in size and is encapsulated by the matrix, especially in the AZ91−1VN alloy. The grain refinement mechanism

of AZ91−0.25VN alloy is thus assumed that the fine AlN phase which is mainly distributed within the grain, could act as heterogeneous nucleation sites for α-Mg grain during the solidification to refine grain. This is consistent with classical nucleation theory and other studies [21,29,30]. With further increasing VN content, some AlN particles become coarser, as shown in Figs. 3(c, d).

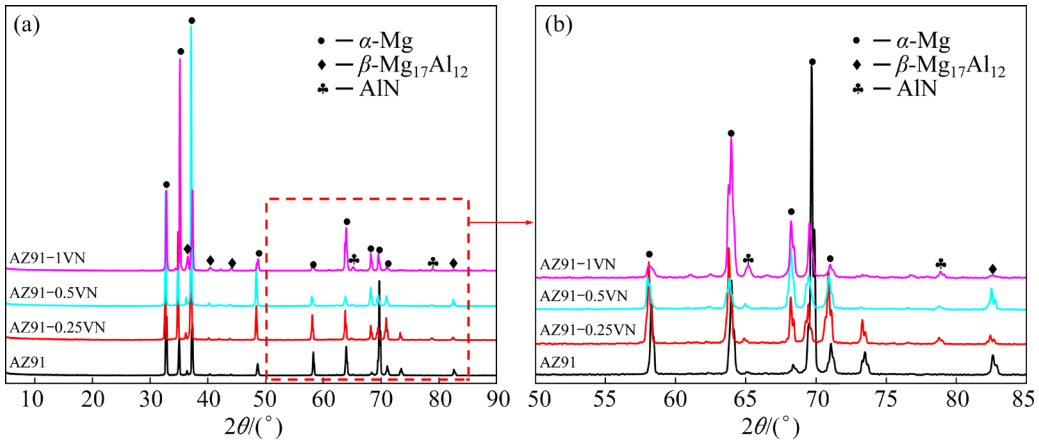

Fig. 2 XRD patterns of as-cast AZ91−xVN alloys (a) and amplified part (b)

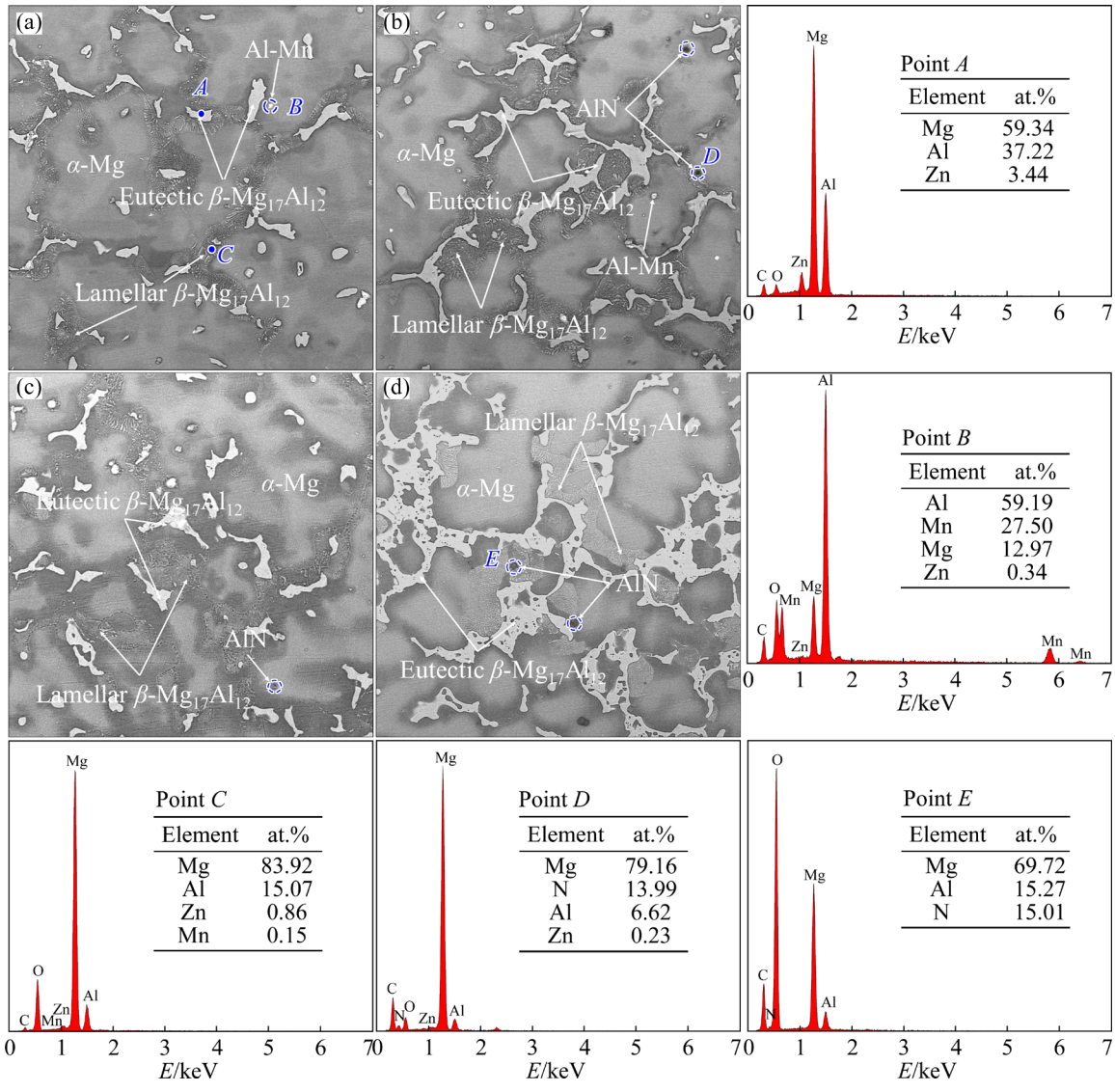

Fig. 3 SEM images of as-cast AZ91−xVN alloys: (a) x=0; (b) x=0.25; (c) x=0.5; (d) x=1

Aggregation of AlN particles at higher VN contents would prevent coarse particles from being active heterogeneous nucleation sites to reduce the grain size and decrease grain refinement efficiency [31,32]. Moreover, because of the constitutional undercooling caused by solute elements ahead of the solid/liquid interface, the addition of Al into Mg alloys results in significant grain refinement [33]. Increasing lamellar β phase with more VN addition implies that more β phase precipitates from matrix, which indicates that more Al element dissolves in α-Mg solid solution during solidification. Meanwhile, less Al element in molten Mg alloy results in the weak effect of constitutional undercooling. So, the existence of VN or AlN would promote the solution of Al element in α-Mg and deteriorate constitutional undercooling effect. Compared with AZ91−0.25VN alloy, the grain sizes of AZ91−0.5VN and AZ91−1VN alloys were coarsened, because Q-values (growth restriction factor) for Al element in the experimental alloys decrease with increasing VN content.

3.2 Corrosion behavior

Figures 4(a, b) show the hydrogen evolution and mass loss rate of AZ91−xVN alloys after immersion in a 3.5 wt.% NaCl solution for 24 h at room temperature, respectively. Initially, the oxide films on the surface protect the matrix, therefore the hydrogen evolves slowly in a short time. After that, the chloride ions penetrate into the film, the active surface area gradually increases, and the corrosion of the matrix accelerates. The amount of hydrogen evolution of the AZ91−0.25VN alloy is (1.75±0.07) mL, which is smaller than that (3.10±0.12) mL of AZ91 alloy. However, when the VN content continues to increase, the amount of hydrogen produces by AZ91−1VN alloy increases significantly to (9.10±0.37) mL, which is 5.2 times that of AZ91−0.25VN alloy. This result indicates that excessive VN leads to worse corrosion resistance of the alloy. Similar trend is observed for the mass loss rate of the samples after immersion for 24 h, and AZ91−0.25VN alloy shows the best corrosion resistance with an average mass loss rate of (0.70±0.03) mg/(cm^2·d).

Figure 5 shows the corrosion morphologies of the four alloys, and it is found that the corrosion starts with pitting corrosion, then spreading around

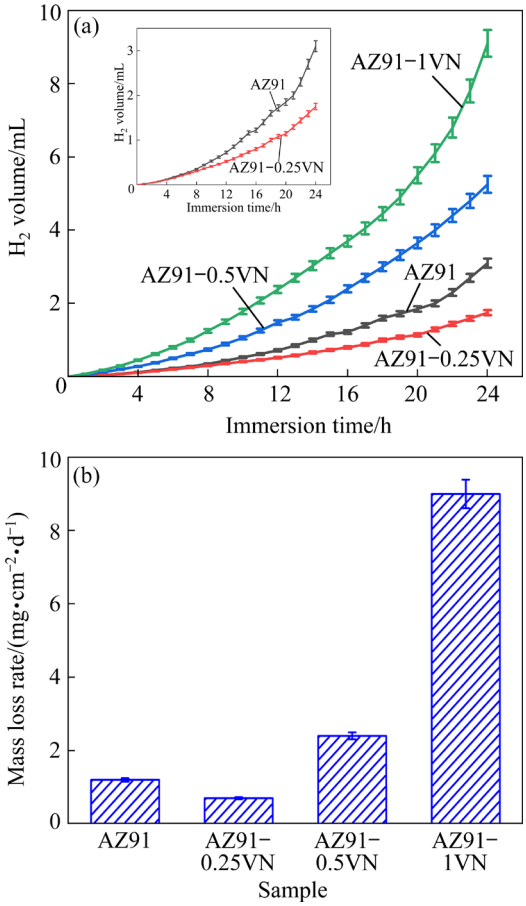

Fig. 4 Hydrogen evolution (a) and mass loss rate (b) of AZ91−xVN alloys immersed in 3.5 wt.% NaCl solution for 24 h

and combining gradually to form the localized corrosion. The AZ91, AZ91−0.25VN, AZ91−0.5VN, and AZ91−1VN alloys are respectively corroded with surface areas of approximately 31.8%, 22.0%, 41.6%, and 59.3%, proofing the best corrosion resistant of the AZ91−0.25VN alloy. The grain size and the amount and distribution of the secondary phase play a crucial role in the corrosion process. SONG and ATRENS [34] suggested that if the volume fraction of the continuously distributed net-like β-$Mg_{17}Al_{12}$ phase was small, the β phase mainly acted as a galvanic cathode and accelerated the corrosion process of the α-Mg matrix; however, for high volume fractions, the β-$Mg_{17}Al_{12}$ phase may act as an anodic barrier and inhibit the overall corrosion of the alloy. Nevertheless, in this experiment, the content of the lamellar β-$Mg_{17}Al_{12}$ phase in the Mg matrix increases with the addition of VN, which shows negative effects on the corrosion behavior, leading to more pitting corrosion spots, forming galvanic corrosion, and

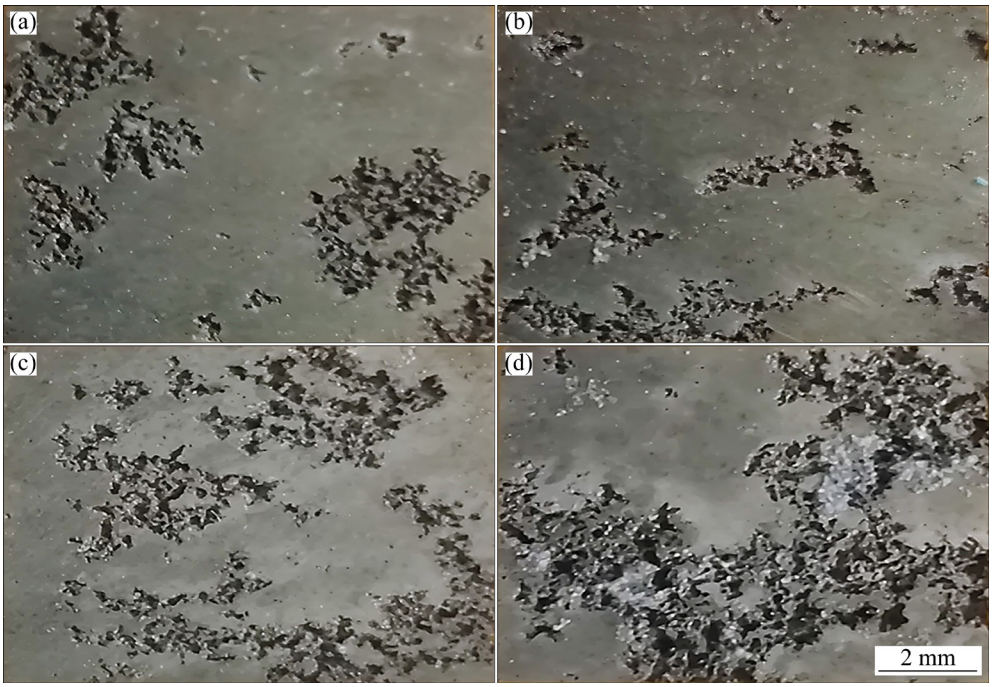

Fig. 5 Macroscopic surface of AZ91−*x*VN alloys immersed in 3.5 wt.% NaCl solution for 24 h: (a) *x*=0; (b) *x*=0.25; (c) *x*=0.5; (d) *x*=1

accelerating the corrosion rate of the Mg matrix [35]. Therefore, among the four alloys, AZ91 alloys with 0.5 wt.% and 1 wt.% VN additions show the worst corrosion resistance. The corrosion resistance of AZ91−0.25VN alloy is improved because less lamellar β-$Mg_{17}Al_{12}$ phase is distributed in the matrix, and the grain refinement enables more grain boundaries to act as a protective barrier [36]. The collection of fine gains formed a protective passive layer, which helps to reduce the corrosion rate in alkaline sodium chloride (NaCl) electrolyte [37].

SEM images and XRD patterns of the corroded products on the alloy surfaces after immersion in 3.5 wt.% NaCl for 24 h are presented in Figs. 6 and 7, respectively. The corrosion product layer is mainly $Mg(OH)_2$ (PDF#76-0667), and the reaction that occurs when alloys are immersed is shown in Reaction (4) [38]:

$$Mg+2H_2O \rightarrow Mg(OH)_2+H_2\uparrow \quad (4)$$

Deep corrosion pits and long cracks (white arrows) exist on the AZ91 alloy surface (Fig. 6(a)), and the long cracks may provide channels for the Cl^- penetration and accelerate the corrosion of the matrix. In the edge area of the pit, the alloy surface is covered by fine chunks of corrosion products without cracks. In the NaCl solution, AZ91−0.25VN alloy reveals more uniform and weaker corrosion behavior. The surface of the alloy is piled up by small chunks of corrosion products, which are uniformly and densely distributed on the matrix, with some fine cracks (as shown by the arrows in Fig. 6(b)). This demonstrates that the corrosion products on the surface of AZ91−0.25VN alloy have high stability and good isolation from the external corrosive environment, which reduces the corrosion rate. When the mass fraction of VN is 0.5% and 1%, the corrosion products become loose and fill with hydrogen pores and the corrosion pits become increasingly deeper (as shown by the arcs and arrows in Figs. 6(c, d)). There are many holes and gaps on the alloy surface, which increase the active area of the Mg matrix and cannot effectively prevent corrosion.

3.3 Electrochemical performance

The polarization curves of the AZ91−*x*VN alloys in the 3.5 wt.% NaCl solution are shown in Fig. 8. All specimens are in an active state during the polarization process. The fitted φ_{corr} and J_{corr} values obtained by using the Tafel extrapolation method are summarized at the top of Fig. 8. The corrosion current density of AZ91−0.25VN alloy is (177.5±3.2) μA/cm^2, which is lower than that

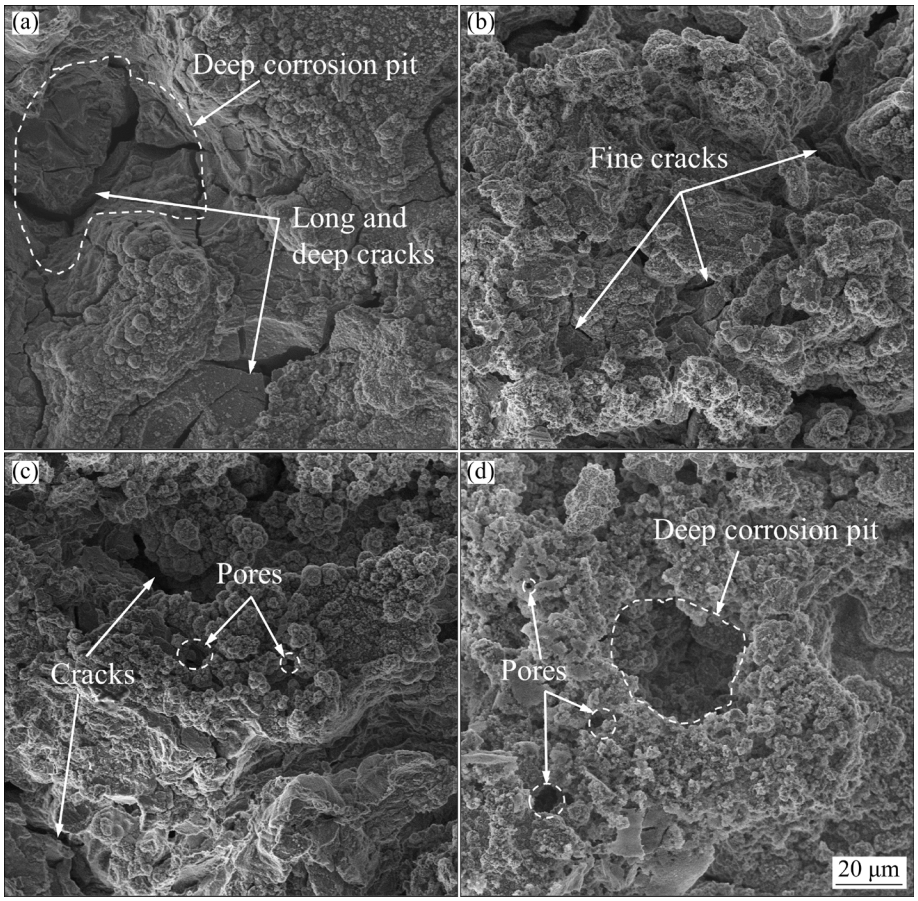

Fig. 6 SEM images of corrosion products on surface of AZ91−xVN alloys: (a) x=0; (b) x=0.25; (c) x=0.5; (d) x=1

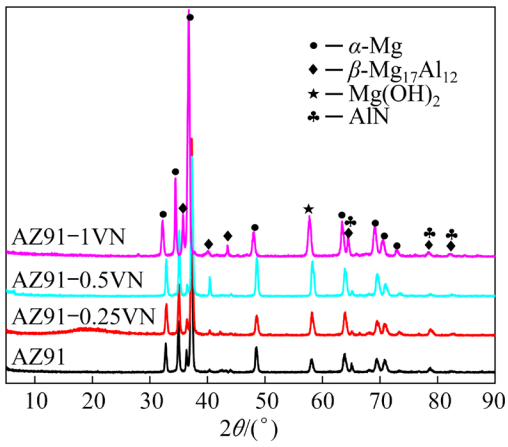

Fig. 7 XRD patterns of corroded products on surface of AZ91−xVN alloys

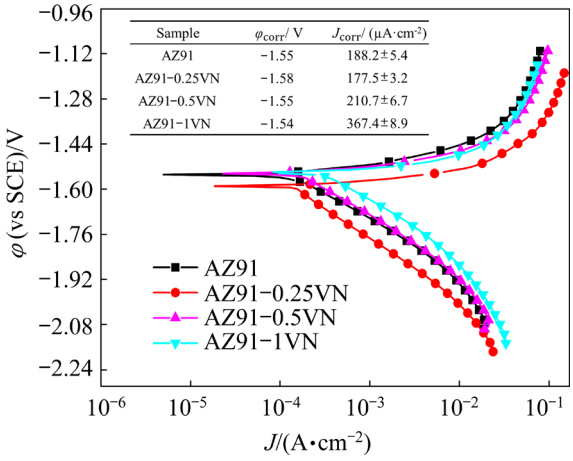

Fig. 8 Polarization curves of AZ91−xVN alloys immersed in 3.5 wt.% NaCl solution in 3.5 wt.% NaCl solution

of other alloys. Based on Faraday's law, corrosion current density is proportional to the corrosion rate [39], indicating that the addition of 0.25 wt.% VN enhances the corrosion resistance of AZ91 alloy. In contrast, the J_{corr} values for AZ91−0.5VN and AZ91−1VN alloys are (210.7±6.7) and (367.4±8.9) μA/cm^2, respectively, showing that the corrosion of AZ91 alloy is accelerated by further increase of VN content. The results are consistent with those obtained by hydrogen evolution and mass loss results.

The corrosion rates obtained by different methods given in Table 1 are plotted in Fig. 9. Obviously, the three different test methods show that the corrosion rate of the specimens increases

Table 1 Hydrogen evolution rate (V_H), hydrogen evolution corrosion rate (P_H), mass loss rate (Δm), corrosion current density (J_{corr}) and corresponding corrosion rate of AZ91−xVN alloys

Sample	V_H/ (mL·cm^{-2}·d^{-1})	P_H/ (mm·a^{-1})	Δm/ (mg·cm^{-2}·d^{-1})	P_W/ (mm·a^{-1})	J_{corr}/ (μA·cm^{-2})	P_i/ (mm·a^{-1})
AZ91	3.10±0.12	7.06±0.28	1.20±0.05	2.52±0.11	188.2±5.4	4.30±0.12
AZ91−0.25VN	1.75±0.07	3.99±0.16	0.70±0.03	1.47±0.06	177.5±3.2	4.06±0.07
AZ91−0.5VN	5.25±0.23	11.96±0.53	2.40±0.10	5.03±0.21	210.7±6.7	4.81±0.16
AZ91−1VN	9.10±0.37	20.74±0.83	9.00±0.39	18.88±0.82	367.4±8.9	8.40±0.21

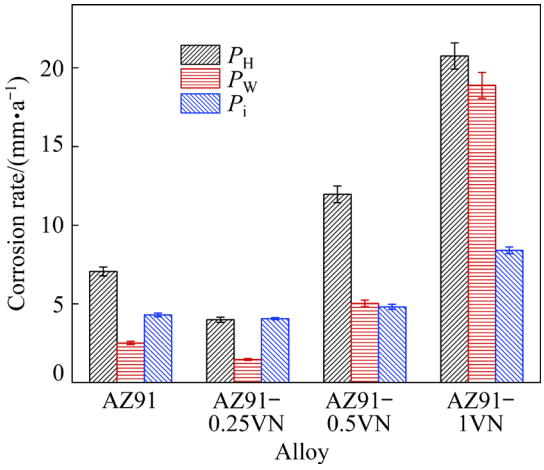

Fig. 9 Corrosion rates of AZ91−xVN alloys by different methods

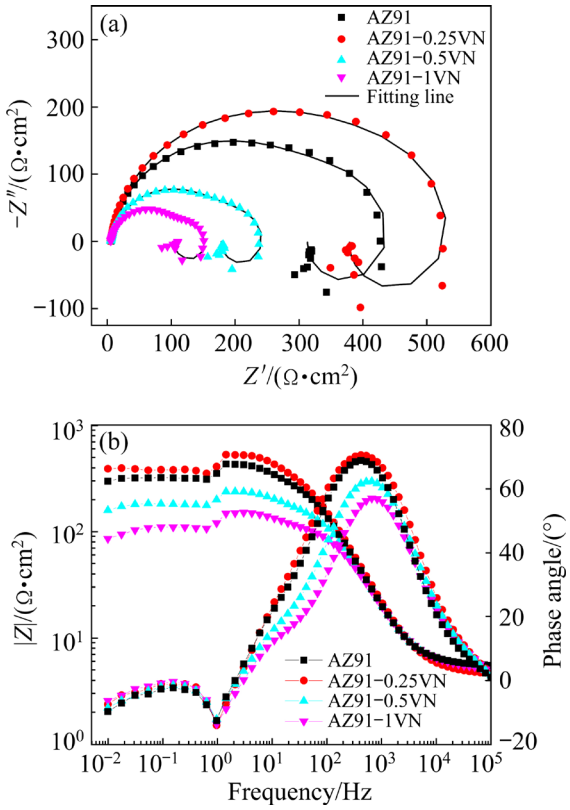

Fig. 10 Nyquist (a) and Bode (b) plots of AZ91−xVN alloys in 3.5 wt.% NaCl solution

as the following order: AZ91−0.25VN, AZ91, AZ91−0.5VN, AZ91−1VN alloys. In addition, variation amplitude of the corrosion rate (P_i) obtained from the polarization curves is substantially lower than the corrosion rate (P_H, P_W) assessed from hydrogen evolution and mass loss rate. There are two possible reasons for the small discrepancy in the corrosion rates measured by the polarization curves [40]: (1) the polarization curve lacks a sufficiently linear Tafel zone, and the immersion time is short; (2) the Mg alloy corrosion is localized rather than homogeneous, which does not fully satisfy the conversion condition of Eq. (3). SONG and ATRENS [41] demonstrated that such deviations were possible.

Figure 10 presents the Nyquist and Bode plots of the studied alloys. The Nyquist plots are composed of a compressed capacitive loop at high and medium frequencies with an inductive loop at low frequencies (Fig. 10(a)). The compressed capacitive loop is respectively related to the corrosion product and the double-electric layer at the high and medium frequencies, while the induction loop at low frequency indicates pitting corrosion and damage to the corrosion layer [42]. The radius of the capacitive loop of AZ91 alloy is obviously lower than that of AZ91−0.25VN alloy, but higher than that of AZ91−0.5VN and AZ91−1VN alloys, suggesting the increasing corrosion resistance of AZ91−0.25VN alloy. The largest impedance exhibits in the Bode plot of the AZ91−0.25VN alloy and the phase responses for the AZ91−0.5VN and AZ91−1VN alloys are lower than those of AZ91 and AZ91−0.25VN alloys (Fig. 10(b)), indicating the highest corrosion resistance of the AZ91−0.25VN alloy [43] and the less coverage of the corrosion product on the surfaces of AZ91−0.5VN and AZ91−1VN alloys [44], respectively.

The EIS fitting for the EIS results was carried out using a three time-constant circuit with an inductive element as shown in Fig. 11. In the equivalent circuit, R_s represents the resistance of solution, R_f and Q_f represent the resistance and capacitance of the corrosion products, R_{ct} and Q_{dl} represent the charge transfer resistance and double-layer capacitance, respectively. L and R_L represent the inductance and inductance impedance, respectively. The fitting results are listed in Table 2 and presented in Fig. 12. Distinct inductances L are observed for all alloys at low frequencies (Table 2), indicating that the corrosion pitting dominated the corrosion process of the alloys in the 3.5 wt.% NaCl solution [42,45]. Obviously, R_f and R_{ct} of the AZ91−0.25VN alloy are higher than those of AZ91 alloy, but those of AZ91−0.5VN and AZ91−1VN alloys are less than the latter, indicating the better corrosion resistance of the AZ91−0.25VN alloy. The fact is consistent with the corrosion rate (Figs. 4 and 9) and the corrosion morphology (Fig. 5). Besides, as shown in Fig. 12, R_f is always higher than R_{ct} for the same alloy in the 3.5 wt.% NaCl solution, reflecting the positive role of the corrosion product film in improving corrosion resistance.

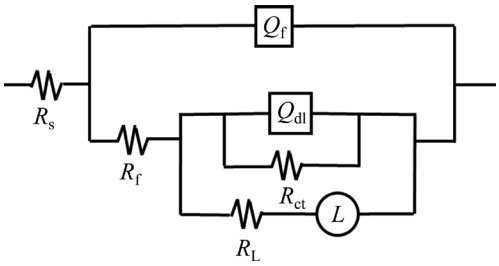

Fig. 11 Equivalent circuit for EIS fitting

Table 2 Electrochemical parameters extracted from equivalent circuit of AZ91−xVN alloys

Alloy	R_s/(Ω·cm^2)	Y_f/(S·s^n·cm^{-2})	n_f
AZ91	5.713	1.642×10^{-5}	0.9228
AZ91−0.25VN	4.802	1.579×10^{-5}	0.9158
AZ91−0.5VN	5.106	2.135×10^{-5}	0.8902
AZ91−1VN	5.358	2.246×10^{-5}	0.8879
Alloy	R_f/(Ω·cm^2)	Y_{dl}/(S·s^n·cm^{-2})	n_{dl}
AZ91	307.5	5.073×10^{-4}	0.7034
AZ91−0.25VN	374.0	3.486×10^{-4}	0.6569
AZ91−0.5VN	172.7	1.141×10^{-3}	0.6530
AZ91−1VN	99.49	3.232×10^{-3}	0.4485
Alloy	R_{ct}/(Ω·cm^2)	R_L/(Ω·cm^2)	L/H
AZ91	166.2	6.634×10^{-3}	13.97
AZ91−0.25VN	207.9	6.439×10^{-3}	16.38
AZ91−0.5VN	90.14	9.700×10^{-4}	7.216
AZ91−1VN	89.71	3.443×10^{-5}	4.956

Y_f and n_f are the admittance and dispersion coefficient of Q_f, respectively; Y_{dl} and n_{dl} are the admittance and dispersion coefficient of Q_{dl}, respectively

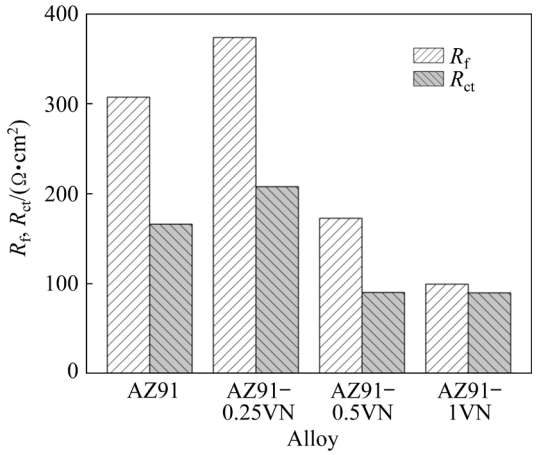

Fig. 12 R_f and R_{ct} of AZ91−xVN alloys immersed in 3.5 wt.% NaCl solution

4 Conclusions

(1) The microstructures of AZ91−xVN (x=0, 0.25, 0.5 and 1, wt.%) alloys are mainly composed of α-Mg, β-$Mg_{17}Al_{12}$, AlN and Al−Mn phases. The average grain sizes of AZ91−xVN alloys firstly decrease and then increase with the addition of VN, and the smallest grain size of 54.52 μm appears in the AZ91−0.25VN alloy.

(2) The corrosion resistance of the AZ91−0.25VN alloy is better than that of the other alloys, which shows the smallest hydrogen evolution amount of 1.75 mL, the smallest mass loss rate of 0.70 mg/(cm^2·d), the largest R_{ct} of 207.9 Ω·cm^2 and the lowest J_{corr} of 177.5 μA/cm^2.

(3) The better corrosion resistance is attributed to the smallest grain size, as the additional grain boundaries can act as the corrosion barriers. Meanwhile, the uniformly distributed and dense protective corrosion products can protect the alloy matrix from subsequent degradation. The corrosion resistance gradually weakens with the further increase of VN content, owing to the formation of lamellar β-$Mg_{17}Al_{12}$ phase, which has a higher galvanic corrosion potential.

Acknowledgments

The authors gratefully acknowledge the financial supports from the National Natural Science Foundation of China (Nos. 52171099, 52105140, 51301025), the Natural Science Foundation of Hunan Province, China (No. 2021JJ40583), the Natural Science Foundation of Changsha City, China (No. kq2014096), the Open Research Fund of Science and Technology Innovation Platform of Key Laboratory of Efficient & Clean Energy Utilization, Education Department of Hunan Province, China (No. 2018NGQ004), and the Innovation Program for Postgraduate of Changsha University of Science and Technology, China (No. SJCX202166)

References

[1] XU Shi-yuan, LIU Chu-ming, WAN Ying-chun, ZENG Guang, GAO Yong-hao, JIANG Shu-nong. Corrosion behaviour of Mg−Gd−Y−Zn−Ag alloy components with different sizes after cooling [J]. Transactions of Nonferrous Metals Society of China, 2021, 31: 1291−1302.

[2] BAZHENOV V E, SAIDOV S S, TSELOVALNIK Y V, VOROPAEVA O O, PLISETSKAYA I V, TOKAR A A, BAZLOV A I, BAUTIN V A, KOMISSAROV A A, KOLTYGIN A V, BELOV V D. Comparison of castability, mechanical, and corrosion properties of Mg−Zn−Y−Zr alloys containing LPSO and *W* phases [J]. Transactions of Nonferrous Metals Society of China, 2021, 31: 1276−1290.

[3] TAN J K E, BALAN P, BIRBILIS N. Advances in LDH coatings on Mg alloys for biomedical applications: A corrosion perspective [J]. Applied Clay Science, 2021, 202: 105948.

[4] ZHU Ji-yuan, JIA Hao-jie, LIAO Kai-jin, LI Xian-xuan. Improvement on corrosion resistance of micro-arc oxidized AZ91D magnesium alloy by a pore-sealing coating [J]. Journal of Alloys and Compounds, 2021, 889: 161460.

[5] WANG Xin, JING Chuan, CHEN Yu-xiang, WANG Xiu-shuang, ZHAO Guang, ZHANG Xing, WU Liang, LIU Xiao-ying, DONG Bi-qin, ZHANG Yu-xin. Active corrosion protection of super-hydrophobic corrosion inhibitor intercalated Mg−Al layered double hydroxide coating on AZ31 magnesium alloy [J]. Journal of Magnesium and Alloys, 2020, 8: 291−300.

[6] CHEN Jun, SONG Ying-wei, SHAN Da-yong, HAN En-hou. In situ growth of Mg−Al hydrotalcite conversion film on AZ31 magnesium alloy [J]. Corrosion Science, 2011, 53: 3281−3288.

[7] METALNIKOV P, BEN-HAMU G, ELIEZER D, SHIN K S. Role of Sn in microstructure and corrosion behavior of new wrought Mg−5Al alloy [J]. Journal of Alloys and Compounds, 2019, 777: 835−849.

[8] LEE D, KIM B, LEE S, BAEK S M, KIM J C, SON H T, LEE J G, LEE K S, PARK S S. Enhanced corrosion resistance of Mg−Sn−Zn−Al alloy by Y microalloying [J]. Scripta Materialia, 2019, 163: 125−129.

[9] DARGUSCH M S, SHI Zhi-ming, ZHU Han-liang, ATRENS A, SONG Gang-ling. Microstructure modification and corrosion resistance enhancement of die-cast Mg−Al−Re alloy by Sr alloying [J]. Journal of Magnesium and Alloys, 2020, 9: 950−963.

[10] ZHANG Tao, SHAO Ya-wei, MENG Guo-zhe, CUI Zhong-yu, WANG Fu-hui. Corrosion of hot extrusion AZ91 magnesium alloy: I—Relation between the microstructure and corrosion behavior [J]. Corrosion Science, 2011, 53: 1960−1968.

[11] SONG Guang-ling, XU Zhen-qing. The surface, micro-structure and corrosion of magnesium alloy AZ31 sheet [J]. Electrochimica Acta, 2010, 55: 4148−4161.

[12] ABDEL-GAWAD S A, SHOEIB M A. Corrosion studies and microstructure of Mg−Zn−Ca alloys for biomedical applications [J]. Surfaces and Interfaces, 2019, 14: 108−116.

[13] ZHANG Cheng, WU Liang, LIU Han, HUANG Guang-sheng, JIANG Bin, ATRENS A, PAN Fu-sheng. Microstructure and corrosion behavior of Mg−Sc binary alloys in 3.5 wt.% NaCl solution [J]. Corrosion Science, 2020, 174: 108831.

[14] CUBIDES Y, KARAYAN A I, VAUGHAN M W, KARAMAN I, CASTANEDA H. Enhanced mechanical properties and corrosion resistance of a fine-grained Mg−9Al−1Zn alloy: The role of bimodal grain structure and β-$Mg_{17}Al_{12}$ precipitates [J]. Materialia, 2020, 13: 100840.

[15] BUZOLIN R H, MOHEDANO M, MENDIS C L, MINGO B, TOLNAI D, BLAWERT C, KAINER K U, PINTO H, HORT N. Corrosion behaviour of as-cast ZK40 with CaO and Y additions [J]. Transactions of Nonferrous Metals Society of China, 2018, 28: 427−439.

[16] BACH L X, SON D L, PHONG M T, THANG L V, BIAN M Z, NAM N D. A study on Mg and AlN composite in microstructural and electrochemical characterizations of extruded aluminum alloy [J]. Composites (Part B): Engineering, 2019, 156: 332−343.

[17] LAZAROVA R, PETROV R H, GAYAROVA V, DAVIDKOV A, ALEXEEV A, MANCHEV M, MANOLOV V. Microstructure and mechanical properties of P265GH cast steel after modification with TiCN particles [J]. Materials & Design, 2011, 32: 2734−2741.

[18] FU H M, ZHANG M X, QIU D, KELLY P M, TAYLOR J A. Grain refinement by AlN particles in Mg−Al based alloys [J]. Journal of Alloys and Compounds, 2009, 478: 809−812.

[19] YANG Chang-lin, ZHANG Bin, ZHAO Dong-chen, LÜ He-bin, ZHAI Tong-guang, LIU Feng. Microstructure and mechanical properties of AlN particles in situ reinforced Mg matrix composites [J]. Materials Science and Engineering A, 2016, 674: 158−163.

[20] ZHAO Hong-liang, ZHAO Zhan-xia, LIU Xu-dong, GUAN Sao-kang. Influence of Mg_3N_2 powder on microstructures and mechanical properties of AZ31 Mg alloy [J]. Journal of

Central South University of Technology, 2008, 15: 459−462.

[21] QIU Wei, LIU Zhi-qiang, YU Rong-zong, CHEN Jian, REN Yan-jie, HE Jian-jun, LI Cong. Utilization of VN particles for grain refinement and mechanical properties of AZ31 magnesium alloy [J]. Journal of Alloys and Compounds, 2019, 781: 1150−1158.

[22] DU Wen-bo, LIU Ke, MA Ke, WANG Zhao-hui, LI Shu-bo. Effects of trace Ca/Sn addition on corrosion behaviors of biodegradable Mg−4Zn−0.2Mn alloy [J]. Journal of Magnesium and Alloys, 2018, 6: 1−14.

[23] GHONEIM A A, FEKRY A M, AMEER M A. Electrochemical behavior of magnesium alloys as biodegradable materials in Hank's solution [J]. Electrochimica Acta, 2010, 55: 6028−6035.

[24] MA Ying-zhong, WANG De-xin, LI Hong-xiang, YANG Chang-lin, YUAN Fu-song, ZHANG Ji-shan. Microstructure, mechanical properties and corrosion behavior of quaternary Mg−1Zn−0.2Ca−*x*Ag alloy wires applied as degradable anastomotic nails [J]. Transactions of Nonferrous Metals Society of China, 2021, 31: 111−124.

[25] SHI Zhi-ming, LIU Ming, ATRENS A. Measurement of the corrosion rate of magnesium alloys using Tafel extrapolation [J]. Corrosion Science, 2010, 52: 579−588.

[26] IRANSHAHI F, NASIRI M B, WARCHOMICKA F G, SOMMITSCH C. Corrosion behavior of electron beam processed AZ91 magnesium alloy [J]. Journal of Magnesium and Alloys, 2020, 8: 1314−1327.

[27] DAHLE A K, LEE Y C, NAVE M D, SCHAFFER P L, STJOHN D H. Development of the as-cast microstructure in magnesium-aluminium alloys [J]. Journal of Light Metals, 2001, 1: 61−72.

[28] CUBIDES Y, KARAYAN A I, ZHAO D X, NASH L, XIE K, CASTANEDA H. New insights on the corrosion mechanism of a peak-aged Mg−9Al−1Zn alloy in a chloride environment [J]. Journal of Alloys and Compounds, 2020, 840: 155786.

[29] GREER A L, BUNN A M, TRONCHE A, EVANS P V, BRISTOW D J. Modelling of inoculation of metallic melts: Application to grain refinement of aluminium by Al−Ti−B [J]. Acta Materialia, 2000, 48: 2823−2835.

[30] LIAO Heng-bin, ZHAN Mei-yan, LI Cheng-bo, MA Zhi-qiang, DU Jun. Grain refinement of Mg−Al alloys inoculated by $MgAl_2O_4$ powder [J]. Journal of Magnesium and Alloys, 2021, 9: 1211−1219.

[31] LIU Peng, GENG Hao-ran, WANG Zhen-qing, ZHU Jian-rong, PAN Fu-sen, DONG Xiao-bin. Effect of AlN on microstructure and mechanical properties of Mg−Al−Zn alloy [J]. Materials Science Forum, 2011, 704: 1095−1099.

[32] JIANG Bin, ZENG Ying, ZHANG Ming-xing, LIAO Ji-chao, PAN Fu-sheng. The effect of addition of cerium on the grain refinement of Mg−3Al−1Zn cast alloy [J]. Journal of Materials Research, 2013, 28: 2694−2700.

[33] LEE Y C, DAHLE A K, STJOHN D H. The role of solute in grain refinement of magnesium [J]. Metallurgical and Materials Transactions A, 2000, 31: 2895−2906.

[34] SONG Guang-ling, ATRENS A. Corrosion mechanisms of magnesium alloys [J]. Advanced Engineering Materials, 1999, 1: 11−33.

[35] YANG Zhen-quan, MA Ai-bin, XU Bing-qian, JIANG Jing-hua, SUN Jia-peng. Corrosion behavior of AZ91 Mg alloy with a heterogeneous structure produced by ECAP [J]. Corrosion Science, 2021, 187: 109517.

[36] PEREIRA G S, KOGA G Y, AVILA J A, BITTENCOURT I M, FERNANDEZ F, MIYAZAKI M H, BOTTA W J, BOSE FILHO W W. Corrosion resistance of WE43 Mg alloy in sodium chloride solution [J]. Materials Chemistry and Physics, 2021, 272: 124930.

[37] RALSTON K D, BIRBILIS N. Effect of grain size on corrosion: A review [J]. Corrosion, 2010, 66: 075005.

[38] CHENG Yuan-fen, DU Wen-bo, LIU Ke, FU Jun-jian, WANG Zhao-hui, LI Shu-bo, FU Jin-long. Mechanical properties and corrosion behaviors of Mg−4Zn−0.2Mn−0.2Ca alloy after long term in vitro degradation [J]. Transactions of Nonferrous Metals Society of China, 2020, 30: 363−372.

[39] LIU Chu-ming, GE Wei-wei, LI Hui-zhong, CHEN Zhi-yong, WANG Rong, GAO Yan-rui. Effect of Er on microstructure and corrosion resistance of AZ91 magnesium alloy [J]. The Chinese Journal of Nonferrous Metals, 2009, 19: 847−853. (in Chinese)

[40] ZHOU Miao, LIU Chu-ming, GAO Yong-hao, XU Shi-yuan, JIANG Shu-nong. Corrosion behavior of Cu-containing AZ31 magnesium alloy [J]. The Chinese Journal of Nonferrous Metals, 2019, 29: 18−26. (in Chinese)

[41] SONG Guang-ling, ATRENS A. Understanding magnesium corrosion—A framework for improved alloy performance [J]. Advanced Engineering Materials, 2003, 5: 837−858.

[42] FENG Hui, LIU Shu-hong, DU Yong, LEI Ting, ZENG Rong-chang, YUAN Tie-chui. Effect of the second phases on corrosion behavior of the Mg−Al−Zn alloys [J]. Journal of Alloys and Compounds, 2017, 695: 2330−2338.

[43] YIN Zheng, HE Ren-hua, CHEN Yang, YIN Zhou, YAN Kun, WANG Kun, YAN Hong, SONG Hong-gun, YIN Cheng-xin, GUAN Hong-yu, LUO Chao, HU Zhi, LUC C. Effects of surface micro–galvanic corrosion and corrosive film on the corrosion resistance of AZ91−*x*Nd alloys [J]. Applied Surface Science, 2021, 536: 147761.

[44] WANG Ying, GU Zheng-peng, LIU Jia, JIANG Jian, YUAN Ning-yi, PU Ji-bin, DING Jian-ning. An organic/inorganic composite multi-layer coating to improve the corrosion resistance of AZ31B Mg alloy [J]. Surface and Coatings Technology, 2019, 360: 276−284.

[45] CHENG Wei-li, MA Shi-chao, BAI Yang, CUI Ze-qin, WANG Hong-xia. Corrosion behavior of Mg−6Bi−2Sn alloy in the simulated body fluid solution: The influence of microstructural characteristics [J]. Journal of Alloys and Compounds, 2018, 731: 945−954.

添加 VN 颗粒的铸态 AZ91 镁合金在 NaCl 溶液中的腐蚀行为

邱 玮[1,2]，李雅文[1,2]，黄 港[1,2]，陈 荐[1,2]，任延杰[1,2]，
黄伟颖[1,2]，陈 维[1,2]，吴堂清[3]，姚茂海[4]，熊爱虎[4]

1. 长沙理工大学 能源与动力工程学院，长沙 410114；
2. 长沙理工大学 能源高效清洁利用湖南省高校重点实验室，长沙 410114；
3. 湘潭大学 材料科学与工程学院，湘潭 411105；
4. 湖南省稀土金属材料研究院 稀土轻合金研究所，长沙 410126

摘 要：采用光学显微镜(OM)、X 射线衍射(XRD)、扫描电子显微镜(SEM)技术和电化学实验研究铸态 AZ91−xVN (x= 0，0.25，0.5，1，质量分数，%)合金的显微组织和腐蚀行为。结果表明，VN 对 AZ91 合金显微组织具有明显的细化和改性作用。随着 VN 颗粒的加入，AZ91 合金的耐腐蚀性能先提高后降低。铸态 AZ91−0.25VN 合金具有最佳的耐腐蚀性能，其腐蚀速率最低(P_W=(1.47±0.06) mm/a)，这主要归因于其具有更多可作为腐蚀屏障的晶界。随着 VN 含量的进一步增加，合金中片状 β-$Mg_{17}Al_{12}$ 析出相的量增加，由于 β 相与 α-Mg 基体易发生电偶腐蚀，合金的耐蚀性能逐渐降低。

关键词：AZ91−xVN 合金；显微组织；晶粒细化；耐腐蚀性能

(Edited by Wei-ping CHEN)